NUWC-NPT TM 932097

NAVAL UNDERSEA WARFARE CENTER DIVISION
NEWPORT, RHODE ISLAND

Technical Memorandum

A LARGE-EDDY SIMULATION OF THE SHEAR-DRIVEN CAVITY FLOW

Date: 31 December 1993

Prepared by: Stephen A. Jordan
Stephen A. Jordan
Launcher Systems
Development Division
Launcher and Missile
Systems Department

Approved for public release; distribution is unlimited.

LIBRARY USE ONLY

Report Documentation Page

Form Approved
OMB No. 0704-0188

1. REPORT DATE	2. REPORT TYPE	3. DATES COVERED
31 DEC 1993	**Technical Memorandum**	**31-12-1993 to 31-12-1993**

4. TITLE AND SUBTITLE	
A Large-Eddy Simulation of the Shear-Driven Cavity Flow	5a. CONTRACT NUMBER
	5b. GRANT NUMBER
	5c. PROGRAM ELEMENT NUMBER
6. AUTHOR(S) **Stephen Jordan**	5d. PROJECT NUMBER **A40100; B40100; and A64962**
	5e. TASK NUMBER
	5f. WORK UNIT NUMBER
7. PERFORMING ORGANIZATION NAME(S) AND ADDRESS(ES) **Naval Undersea Warfare Center Division,Newport,RI,02841**	8. PERFORMING ORGANIZATION REPORT NUMBER **TM 932097**
9. SPONSORING/MONITORING AGENCY NAME(S) AND ADDRESS(ES)	10. SPONSOR/MONITOR'S ACRONYM(S)
	11. SPONSOR/MONITOR'S REPORT NUMBER(S)

12. DISTRIBUTION/AVAILABILITY STATEMENT
Approved for public release; distribution unlimited

13. SUPPLEMENTARY NOTES
NUWC2015

14. ABSTRACT
The three-dimensional shear-driven cavity flow is numerically investigated at Reynolds numbers of 5000 and 10,000. This investigation focuses on the unsteadiness and turbulent characteristics of the flow. At the moderate Reynods number (Re = 5000) where the cavity flow is fully laminar, a direct numerical simulation (DNS) is used; at the higher Reynolds number (Re = 10,000), large-eddy simulation (LES) methodology is used to predict the cavity flow. Establishing a suitable form for the subgrid scale (SGS) turbulence model in this complex flow is guided by the DNS results at Re = 5000. Additionally, the SGS model is verified against DNS results at Re = 7500, where the cavity flow is known through experimentation to be locally transitional. The LES results verify the published experimental evidence, as well as introduce new flow features within the cavity.

15. SUBJECT TERMS
cavity flow; Reynolds number; :ES; Large-eddy simulation

16. SECURITY CLASSIFICATION OF:			17. LIMITATION OF ABSTRACT	18. NUMBER OF PAGES	19a. NAME OF RESPONSIBLE PERSON
a. REPORT **unclassified**	b. ABSTRACT **unclassified**	c. THIS PAGE **unclassified**	**Same as Report (SAR)**	**28**	

Standard Form 298 (Rev. 8-98)
Prescribed by ANSI Std Z39-18

ABSTRACT

The three-dimensional shear-driven cavity flow is numerically investigated at Reynolds numbers of 5000 and 10,000. This investigation focuses on the unsteadiness and turbulent characteristics of the flow. At the moderate Reynods number (Re = 5000) where the cavity flow is fully laminar, a direct numerical simulation (DNS) is used; at the higher Reynolds number (Re = 10,000), large-eddy simulation (LES) methodology is used to predict the cavity flow. Establishing a suitable form for the subgrid scale (SGS) turbulence model in this complex flow is guided by the DNS results at Re = 5000. Additionally, the SGS model is verified against DNS results at Re = 7500, where the cavity flow is known through experimentation to be locally transitional. The LES results verify the published experimental evidence, as well as introduce new flow features within the cavity.

ADMINISTRATIVE INFORMATION

This memorandum was prepared under FY93 Project Numbers A40100 and B40100, supported by the Office of Naval Research (L. P. Putrell, Scientific Officer) and Project Number A64962, supported by the Naval Undersea Warfare Center Division Newport's Independent Research Program (K. Lima, Coordinator).

The author of this memorandum is located at the Naval Undersea Warfare Center Division, Newport, RI 02841-1708.

TABLE OF CONTENTS

Page

LIST OF ILLUSTRATIONS iv

INTRODUCTION 1

BASIC MODEL PROBLEM INCLUDING EXPERIMENTAL OBSERVATIONS 2

GOVERNING EQUATIONS AND METHOD OF SOLUTION 4

SUBGRID TURBULENCE MODEL 5

RESULTS AND DISCUSSION 5
- DNS Results 7
- LES Results 10

CONCLUSIONS 20

REFERENCES 21

LIST OF ILLUSTRATIONS

Figure		Page
1	Sketch of the Basic Features of Recirculation in the Two-Dimensional Shear-Driven Cavity Flow Problem	2
2	Sketch of the Taylor-Görtler-Like Vortex Pairs as Observed in the Flow Visualization Experiments	3
3	Model Problem for Present DNS and LES Predictions of the Shear-Driven Cavity Flow.	6
4	Snapshots of the Unsteady Shear-Driven Cavity Flow at Relative Time $t = 15.0$; (a) Recirculation at Mid-Span, (b) TGL Vortices at Plane $x = 0.77$ and (c) Spanwise Static Pressure Contours	8
5	Snapshots of the Unsteady Shear-Driven Cavity Flow at Relative Time $t = 181.0$; (a) Recirculation at Mid-Span and (b) TGL Vortices at Plane $x = 0.77$	9
6	Spanwise Distribution and Streamwise Extent of TGL Vortices at Completion of DNS Computation ($t = 3$ min)	9
7	Time Traces (a) and (c) and Power Spectra (b) and (d) of Horizontal and Vertical Velocity Components Near the Downstream Free Shear Layer for Test Case $Re = 5000$	11
8	Quantitative Comparisons of the DNS Results and Experimental Data [26] in Terms of the Centerline Mean Velocities at the Cavity Mid-Span Plane.	12
9	Distribution of Correlation Coefficient c_{12} Using $C_s = 0.1$ and Parameters $m = 8.0$ and $n = 0.14$ in Turbulence Length Scale Definition. Correlation Computed from DNS Data Taken at Completion of Test Case $Re = 5000$	12
10	Turbulent Eddy Viscosity Level (Normalized by the Kinematic Viscosity) Computed from DNS Taken at Completion of Simulation; (a) $Re = 5000$ and (b) $Re = 7500$	13
11	Velocity Vectors Illustrating (a) Regions of the Downstream Secondary Eddy and (b) TGL and Corner Vortices for LES Test Case $Re = 10{,}000$ at Relative Time $t = 6.5$	13

LIST OF ILLUSTRATIONS (Cont'd)

Figure		Page
12	Stream Function Contours Showing the Downstream and Upstream Secondary Eddies of the Shear-Driven Cavity at Re = 10,000; Time t = 6.5	14
13	Stream Function Contours Showing the TGL and Corner Vortices of the Shear-Driven Cavity at Re = 10,000; Time t = 6.5	15
14	Five Sets of Particle Traces Illustrating the Interaction Among the Primary Recirculation Vortex, Downstream Secondary Eddy, and TGL and Corner Vortices of the LES Computation at Relative Time t = 6.5	16
15	Comparison of LES and Experimental Results [12] in Terms of Centerline Mean Velocity Profiles; Simulation Profile at K15 Plane and Experimental Data Measured at Mid-Span Plane	18
16	Profiles of Centerline Horizontal and Vertical RMS Velocity Fluctuations; LES Profiles Are at the K15, End, and Mid-Span Planes While Experimental Data Are at the Mid-Span Plane of Cavity with SAR = 1:1	18
17	Power Spectra of Velocity Components Near the Downstream Free Shear Layer; (a) Horizontal, (b) Vertical	19
18	Distribution of the (a) Vertical RMS Fluctuations and (b) u'v' Shear Stress Component at the K15 Plane	19

INTRODUCTION

For more than three decades, the shear-driven cavity flow problem has served as an excellent test case for verifying new or improved numerical solution techniques of incompressible flows. Usually, the test case involves simulating a two-dimensional (2D) cavity flow at a low Reynolds number (Re $\leq$ 1000). Under these conditions, the flow is strictly laminar and steady. The primary purpose of the simulations is to illustrate the rapid speed of convergence to steady state and the solution method's ability to capture the basic features of the flow. Some 2D simulations (for example, Ghia et al. [1] and Gustafson and Halasi [2]) include a discussion of the flow characteristics and have revealed important salient features of the steady flow at much higher Reynolds numbers (Re $\leq$ 10,000). The extensive results of Ghia et al., in particular, serve most often as a base for comparison of new 2D predictions because of the fine grid resolution they used at the corresponding Re. Only a few numerical studies have reported the turbulent characteristics of the shear-driven cavity flow (Gosman et al. [3], Young et al. [4], Ideriah [5], and Gaskell and Lau [6], for instance). Each study simulated a 2D geometry with the turbulence fully modeled. Treatment of the results was qualitative, meaning that the investigators validated the particular numerical scheme or evaluated various turbulence models. Separate studies showing the flow evolution in the 2D cavity under an impulsively started lid and an oscillating lid were reported by Soh and Goodrich [7]. In both simulations, the flow was laminar (Re = 400) and the predictions continued until steady-state. Published results from three-dimensional (3D) simulations include those of Moin and Kim [8], Freitas et al. [9], and Prasad et al. [10], where the Reynolds number was restricted to low-to-moderate values (Re $\leq$ 3200). There, the flow was also laminar. The simulations showed the appearance of pairs of quasi-steady and unsteady spanwise Taylor-Görtler-like (TGL) vortices along the cavity bottom. Besides validating the conservativeness of their particular solution technique, each revealed this important 3D characteristic, which had been observed experimentally but not numerically.

In addition to furnishing us with a classic problem for validating solution techniques of incompressible flows, the predominant features of the shear-driven cavity flow also have important physical significance in view of engineering design. For example, the main flow characteristics created by 3D geometries such as recessed cavities, recurrent ribs or slots and curved ducts, for the purposes of mass and/or energy exchange, are similar to those of this model problem. Given this fact, the objective of the present work is to identify and characterize, through numerical simulation, the unsteadiness and turbulence in a 3D shear-driven cavity flow. This numerical investigation is presented for Reynolds numbers of 5000 and 10,000. Numerical results of the unsteady and laminar flow characteristics at much lower Reynolds numbers (Re = 2000 and Re = 3200) were presented by Jordan and Ragab [11].

For the moderate Reynolds number test case (Re = 5000) where the flow is unsteady and laminar, the computation was a direct numerical simulation (DNS). At the higher Re, the prediction method was a large-eddy simulation (LES). Although extensive experimental results of the high-Re cavity flow have been reported for just over 10 years now, this LES investigation is a first attempt to study the turbulent flow characteristics numerically. Before deriving any new unsteady or turbulent flow features, however, the numerical results are first scrutinized thor-

oughly against the experimental evidence. Thus, this LES computation verifies the published experimental data as well as introduces new characteristics about the flow.

BASIC MODEL PROBLEM INCLUDING EXPERIMENTAL OBSERVATIONS

Geometrically, the classic 2D problem consists of a closed cavity of unit height (H) and unit width (W) with a lid moving horizontally at unit velocity (U). The Reynolds number is defined as $Re = UW/\nu$, where ν is the kinematic viscosity. The associated recirculation flow is characterized basically by a primary vortex, a downstream secondary eddy, an upstream secondary eddy, and an upper secondary eddy. These basic features are sketched in figure 1. The upper

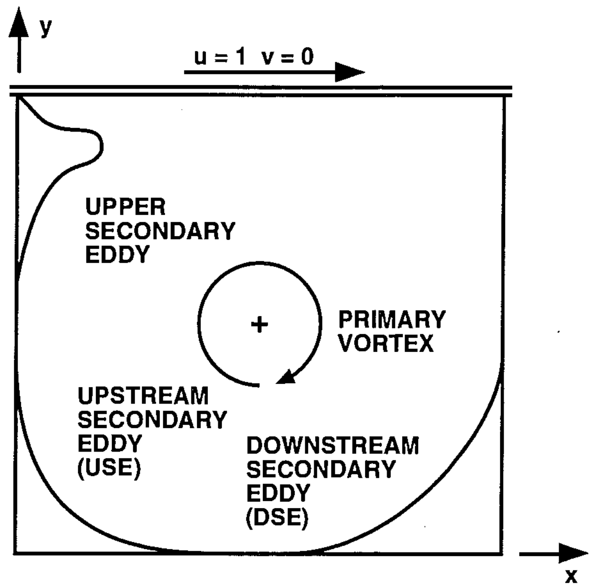

Figure 1. Sketch of the Basic Features of Recirculation in the Two-Dimensional Shear-Driven Cavity Flow Problem

secondary eddy appears at $Re \geq 3200$. At higher Re (≥ 5000) the 2D predictions show a tertiary eddy in each of the lower corners. Based on the experimental observations of Koseff and Street [12] of the 3D cavity flow, these tertiary eddies are unique only to the 2D simulations. From their observations, Koseff and Street also reported that the basic features of the recirculation flow in figure 1 are nearly self-similar throughout the cavity span at high Reynolds numbers where the flow is locally transitional.

In the 3D cavity new vortical structures are formed. In a spanwise plane, there are several pairs of TGL vortices and a lower corner vortex at the end-walls (see sketch in figure 2). According to Koseff and Street [13] and Prasad et al. [10], the impetus for manifesting the TGL vortices is the instability of the concave free shear layer that separates the primary vortex from the downstream secondary eddy. Generation of the vortices occurs just above the concave surface, much like the experimental observations of Taylor [14] for the flow between rotating

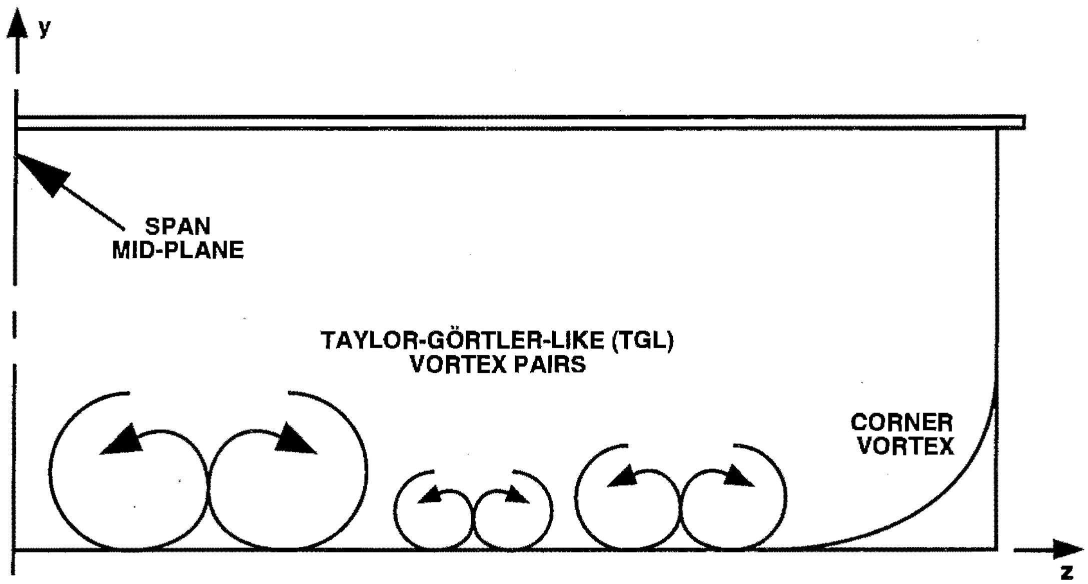

Figure 2. Sketch of the Taylor-Görtler-Like Vortex Pairs as Observed in the Flow Visualization Experiments [12]

cylinders and also the concave boundary layer investigated by Görtler [15]. The size and number of pairs of TGL vortices depends strongly on the Reynolds number and the cavity spanwise aspect ratio (SAR). In the flow visualization results reported by Rhee et al. [16] for Re $\leq$ 6000 and SAR = 3.0, the spanwise flow maintained symmetry about the mid-span plane. Although the TGL vortices meander slowly along the cavity bottom at moderate Re, Koseff and Street [13] noted that their basic spanwise flow character still remains symmetric. The other important feature in the spanwise direction is the lower corner vortex. The origin of this flow structure was explained by Koseff and Street [17] after they examined the experimental results of de Brederoede and Bradshaw [18]. Manifestation of this vortex is a consequence of the shear and pressure force adjustment in the streamwise recirculating flow caused by the no-slip condition along the spanwise end-wall. Like the TGL vortices, the corner vortex becomes unsteady at moderate Reynolds numbers (Re $\geq$ 3200). The size and extent of the corner vortex strongly influences the TGL vortices. Thus, the numerical simulations must provide sufficient resolution, spatially and temporally, to capture its characteristics accurately.

Experimental observations show the first sign of turbulence taking place within the free shear layer that lies between the primary vortex and downstream secondary eddy. This local transition to turbulence occurs at a Reynolds number somewhere between 6000 and 8000 [13]. The flow within that region is unsteady. If the Reynolds number is increased, the onset of turbulence diffuses the TGL vortices such that their deterministic structure becomes obscured. At Re = 10,000, frequency spectra of both the horizontal and vertical fluctuations within the region of the free shear layer display an inertial subrange. It should be noted that the visualization results show the flow within the free shear layer at Re = 10,000 as being still transitional.

GOVERNING EQUATIONS AND METHOD OF SOLUTION

The governing LES equations of the resolvable field are the spatially filtered incompressible Navier-Stokes equations:

$$\frac{\partial \overline{u}_i}{\partial t} + \frac{\partial}{\partial x_j}\left(\overline{u}_i \overline{u}_j\right) = -\frac{\partial p}{\partial x_i} + \frac{1}{\mathrm{Re}} \frac{\partial^2 \overline{u}_i}{\partial x_j \partial x_j} + \frac{\partial \tau_{ij}}{\partial x_j}, \tag{1}$$

$$\frac{\partial \overline{u}_i}{\partial x_i} = 0. \tag{2}$$

where p is the pressure, and t_{ij} is the subgrid scale stress tensor, which is defined as $\tau_{ij} = \overline{u}_i \overline{u}_j - \overline{u_i u_j}$.

The system of equations is time-advanced according to a variant of the fractional-step method [19]. The Crank-Nicolson scheme is applied to the viscous terms to eliminate the viscous stability restriction. An explicit three-step third-order-accurate Runge-Kutta (R-K) scheme is used for the convective terms instead of the more popular Adams-Bashforth method (see Clark et al. [20], for example). This is done because the Adams-Bashforth method is weakly unstable when applied to the linear convection equation. Also, the explicit form of the R-K scheme easily permits high-order spatial differences. In this application of the LES approach, the convective terms are spatially discretized by third-order upwind-biased finite differences, while the diffusive terms are differenced by second-order central differences. At the points next to the wall boundaries, exterior points necessary to complete the upwind differencing are obtained through extrapolation of the interior field points. All terms in Poisson's equation for solution of the pressure variable are central differenced to the second order. Strong coupling between the pressure and velocity components is maintained through a fourth-order-accurate compact differencing scheme for the pressure gradient in the velocity update equation. This discretization scheme provides an overall method that is second-order-accurate in both space and time.

The velocity components are collocated with the grid points to permit easy development of a set of wall boundary conditions for the velocity field. Approximate-factorization (A-F) is applied for solution of the intermediate velocity components. The pressure field is staggered from the velocity field to eliminate spurious oscillations in the flow solutions [21]. No boundary condition is required for the pressure variable. Poisson's equation for solution of the pressure variable is recast into a residual form and solved by a variant of the modified strongly implicit procedure [22]. This procedure is implemented as an implicit elliptic solver of a planar surface that moves through the volume. After the initial time steps, only a few iterations on the pressure variable are necessary to satisfy the incompressibility constraint at each of the following time steps. Extensive details of these numerics, along with several test cases, can be found in Jordan and Ragab [11].

SUBGRID TURBULENCE MODEL

For the computations of the turbulent shear-driven cavity flow, the Smagorinsky eddy viscosity model [23] was implemented to represent the subgrid scale (SGS) turbulence. In tensor notation the Smagorinsky model is:

$$\tau_{ij} - \tfrac{1}{3}\delta_{ij}\tau_{kk} = 2\nu_T S_{ij}, \tag{3}$$

$$S_{ij} = \tfrac{1}{2}\left(u_{i,j} + u_{j,i}\right), \tag{4}$$

$$\nu_T = L^2\sqrt{2S_{ij}S_{ij}}, \tag{5}$$

$$L = C_s\left[1 - \exp\left(-y^+ / A^+\right)^m\right]^n \left(\Delta_1\Delta_2\Delta_3\right)^{1/3}. \tag{6}$$

In this model, L is the turbulent characteristic length scale. Modification of the length scale by a form of van Driest damping [24] was necessary to account for the effects of the solid wall boundaries. The length parameter y^+ is the minimum field value of $y^+ = y\sqrt{\tau_\ell / \rho} / \nu$, where τ_ℓ is the magnitude of the local shear stress. The subscripts 1, 2, and 3 of the filter width D permit versatile filtering for modeling anisotropic flows. As a minimum $\Delta_i = 2h_i$, where h_i is the grid spacing in the i direction. The exponents m and n in the van Driest damping function were determined by analyzing the DNS results and by qualitative comparisons to the published experimental measurements. The importance of including van Driest damping in the Smagorinsky model became apparent after applying the model to the DNS results at Re = 5000 without the damping modification. The model repeatedly showed high levels of turbulent eddy viscosity near the upper half of the downstream wall. At times, these levels reached the same order of magnitude as the kinematic viscosity, marking the onset of turbulence. Based on the experimental observations, however, this is a false indication. As discussed earlier, the flow visualization results suggest that initial signs of turbulence occur within the free shear layer between the primary vortex and the downstream secondary eddy located near the lower half of the downstream wall. By damping the length scale according to a form of van Driest, the near-wall turbulent eddy viscosity was reduced and the modified model agreed qualitatively with the experimental evidence. This issue is addressed further in the next section.

RESULTS AND DISCUSSION

This section presents the unsteady and turbulent flow results from a numerical investigation of the 3D shear-driven cavity and includes comparisons with the published experimental observations and measurements. This investigation is of a cavity with SAR = 3.0. Reynolds numbers of 5000 and 10,000 were simulated. The cavity geometry was modeled as unit streamwise (x-direction) and normal (y-direction) lengths; W = 1.0 and H = 1.0 (see figure 3). Based on the

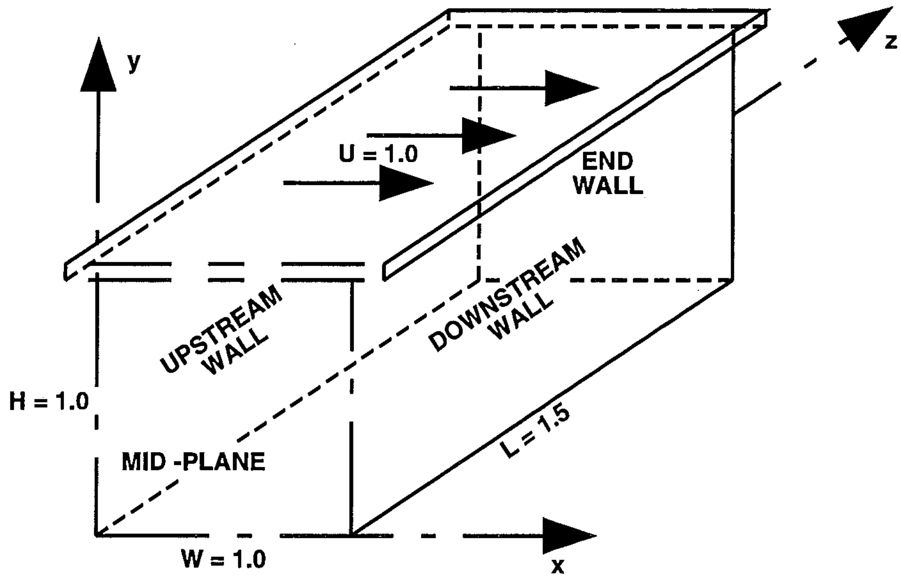

Figure 3. Model Problem for Present DNS and LES Predictions of the Shear-Driven Cavity Flow

published flow visualization data [13,16,17] for Re $\leq$6000 and previous simulations [9,10,11] for Re = 3200, only one-half of the cavity span was modeled. Thus, the spanwise (z-direction) length is 1.5 times that of the streamwise length, with one boundary modeled as a plane of symmetry at mid-span (z = 0.0) and the other a solid end-wall (z = 1.5). For the Re = 10,000 simulation, a localized effect of the symmetry plane assumption on the numerical results will be shown. The lid moved horizontally with unit velocity (U_L=1.0); hence, the Reynolds number is simply the inverse of the kinematic viscosity. The no-slip condition was enforced along all boundaries except at the mid-span plane, which was treated numerically as a plane of symmetry. All grids selected had uniform point spacing.

Each simulation was initialized by an impulsively started lid. Inasmuch as the convective terms are time-split by the R-K technique, extremely small time increments were not necessary early in the simulation to maintain stability. For both simulations, a low CFL value of 0.5 was chosen to ensure proper temporal resolution of the flow unsteadiness rather than controlling numerical stability. It was found that CFL values near the stability limit distorted the TGL vortex structures. Herein, computational results, which are labeled t = 0.0, represent solutions that had been time-advanced until the effects of the impulsively started lid on the flow evolution became negligible. In both simulations, this time was approximately 1 minute.

In view of the experimental evidence, the cavity flow is entirely laminar at low to moderate Reynolds numbers (Re $\leq$ 5000). Therefore, the simulation at Re = 5000 is essentially a DNS prediction. The importance of the DNS results with respect to the LES methodology lies in improving the estimate of the turbulence length scale; specifically, determining suitable values

for the exponents (m and n) in the van Driest damping function and for the Smagorinsky constant (C_S). The procedure used here closely follows the SGS turbulence model development by Clark et al. [20]. The model parameters were judged according to the best overall set of coefficients attained from correlations between the exact (computed from the DNS data) and the model results in terms of the SGS stresses t_{ij}. The correlation coefficient is defined as $< c_{ij} >=< e_{ij}m_{ij} > / < e_{ij}^2 >^{1/2}< m_{ij}^2 >^{1/2}$ where $< e_{ij} >$ and $< m_{ij} >$ are the spatially ensemble-averaged exact and model t_{ij} components, respectively. Inasmuch as the spanwise flow direction was assumed to be homogeneous, only the coefficients c_{11}, c_{22}, and c_{12} were determined. In addition, only positive values of these coefficients were considered in the model evaluation. Before the model was implemented in the Re = 10,000 simulation, its quality was checked against the published experimental observations. In this section, we will show that the definition in equation (6) for the turbulence length scale, along with its associated constants, is acceptable for the shear-driven cavity flow problem at the simulated Reynolds numbers. Although designing a proper form for the turbulence model was focused on the DNS results at Re = 5000, the model quality was also checked at a higher Reynolds number where the flow is locally transitional.

DNS RESULTS

For the test case of Re = 5000, DNS computations were performed over a 65 x 65 x 65 (x, y, z-direction) uniform grid. Based on the grids used in previous simulations of 3D cavity flow [9,10,11], this mesh resolution is adequate for this Reynolds number. The simulation was carried out for approximately 4 minutes. Figures 4a and 4b show a set of snapshots of the unsteady flow results at time t = 15.0. This relative time corresponds to an actual time of over 1 minute since impulsive start of the lid. The velocity vectors in figure 4a represent the recirculation flow at the mid-span plane, whereas those in figure 4b depict the spanwise flow at plane x = 0.77. For clarity, each of the velocity vectors is normalized by its own magnitude. Although there seems to be 3D effects in the upper half of the spanwise plane, their magnitudes are small and therefore have little significance for the flow structure. At this instant in time (t = 15.0), the three basic features of the recirculation flow that are common to the 2D simulations are distinctly visible. Likewise, the primary vortex core is positioned close to the cavity center. This agreement is due primarily to the minimal influence of the spanwise flow on the mid-span recirculation flow (see figure 4b). The spanwise flow vectors show four TGL vortices of nearly the same height that lie fully within the cavity span. Since the static pressure attains a minimum within the vortex core, contours of the pressure variable can verify the existence of each vortex. An example of this is portrayed in figure 4c. A few grid lines are superimposed over the pressure contours and the corresponding velocity vectors to help identify each respective vortex.

At time t = 181.0, the snapshots paint a very different picture (see figures 5a and 5b). The 3D effects on the basic recirculating flow features are clearly displayed. For example, the TGL vortex that straddles the mid-span plane severely distorts the basic structure of the downstream secondary eddy (DSE). Throughout most of the simulation, a TGL vortex structure straddled the mid-span plane, which precluded development of the local DSE. According to the experimental

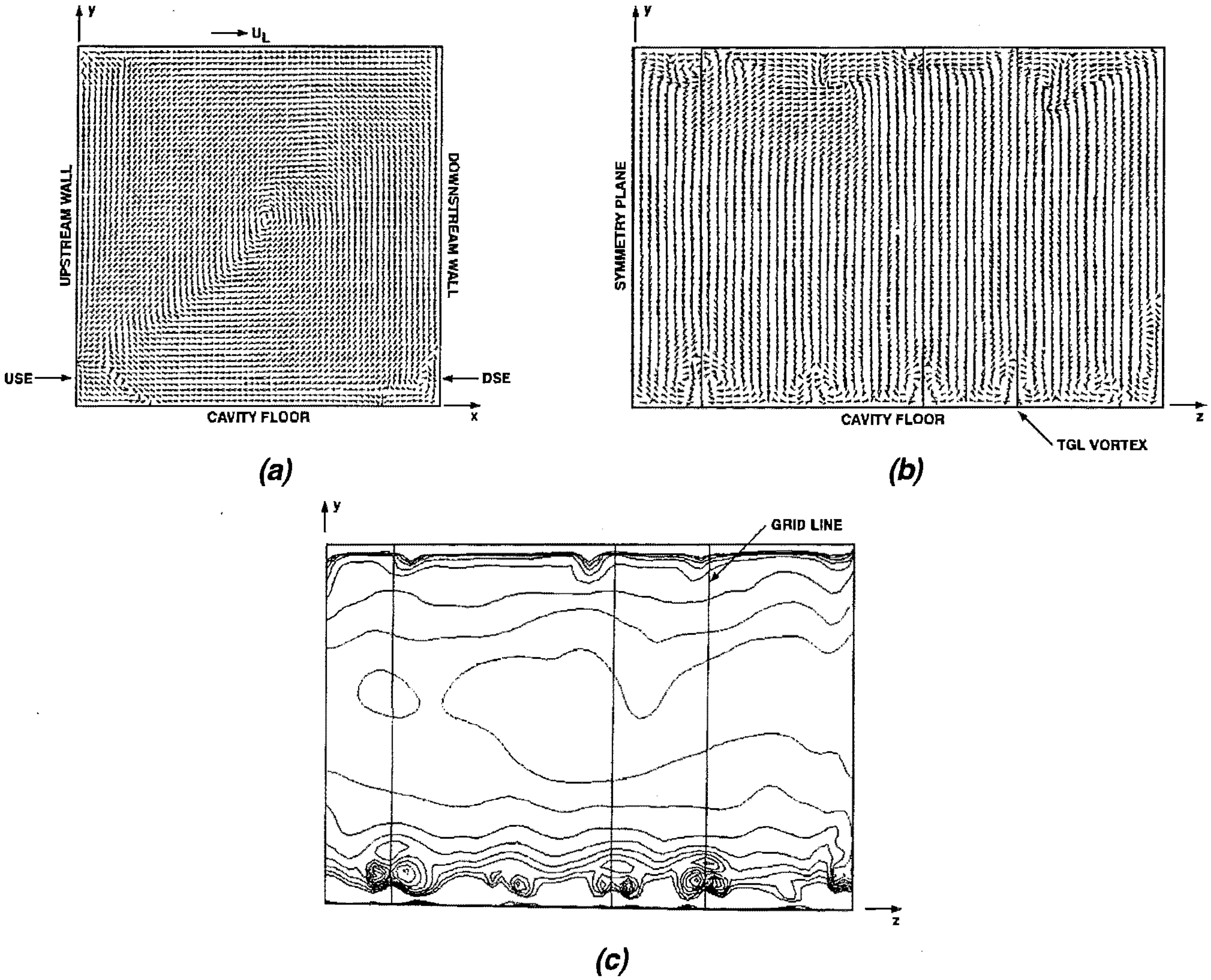

Figure 4. Snapshots of the Unsteady Shear-Driven Cavity Flow at Relative Time t = 15.0; (a) Recirculation at Mid-Span, (b) TGL Vortices at Plane x = 0.77 and (c) Spanwise Static Pressure Contours

results [16], eight pairs of TGL vortices were visualized at Re = 3200, and 11 vortex pairs at Re = 6000. At Re = 5000 we found nine vortex pairs; one typically straddling the mid-span plane and four others spanning the cavity floor. This result is shown in figure 6, which is a plot of the x-vorticity at completion of the simulation (t =181.0). Notice that the streamwise extent of each vortex pair does not strongly interact with the upstream secondary eddy (USE). This is because the flow process of fluid entrainment from the primary vortex to sustain the structural integrity of each TGL vortex is terminated once the primary vortex separates upstream. Particle traces that illustrate this flow process are presented in the next section.

In the literature, neither velocity time traces nor mean velocity experimental data appear for the 3D cavity flow at Re = 5000 and SAR = 3.0. Here, shown in figures 7a through 7d are time

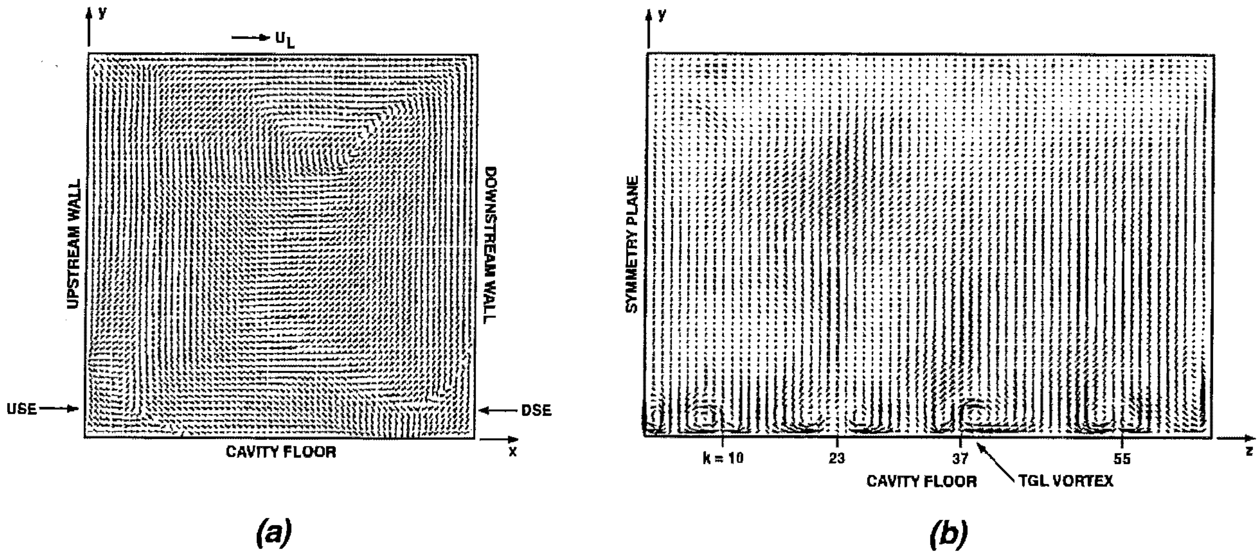

Figure 5. Snapshots of the Unsteady Shear-Driven Cavity Flow at Relative Time t = 181.0; (a) Recirculation at Mid-Span and (b) TGL Vortices at Plane x = 0.77

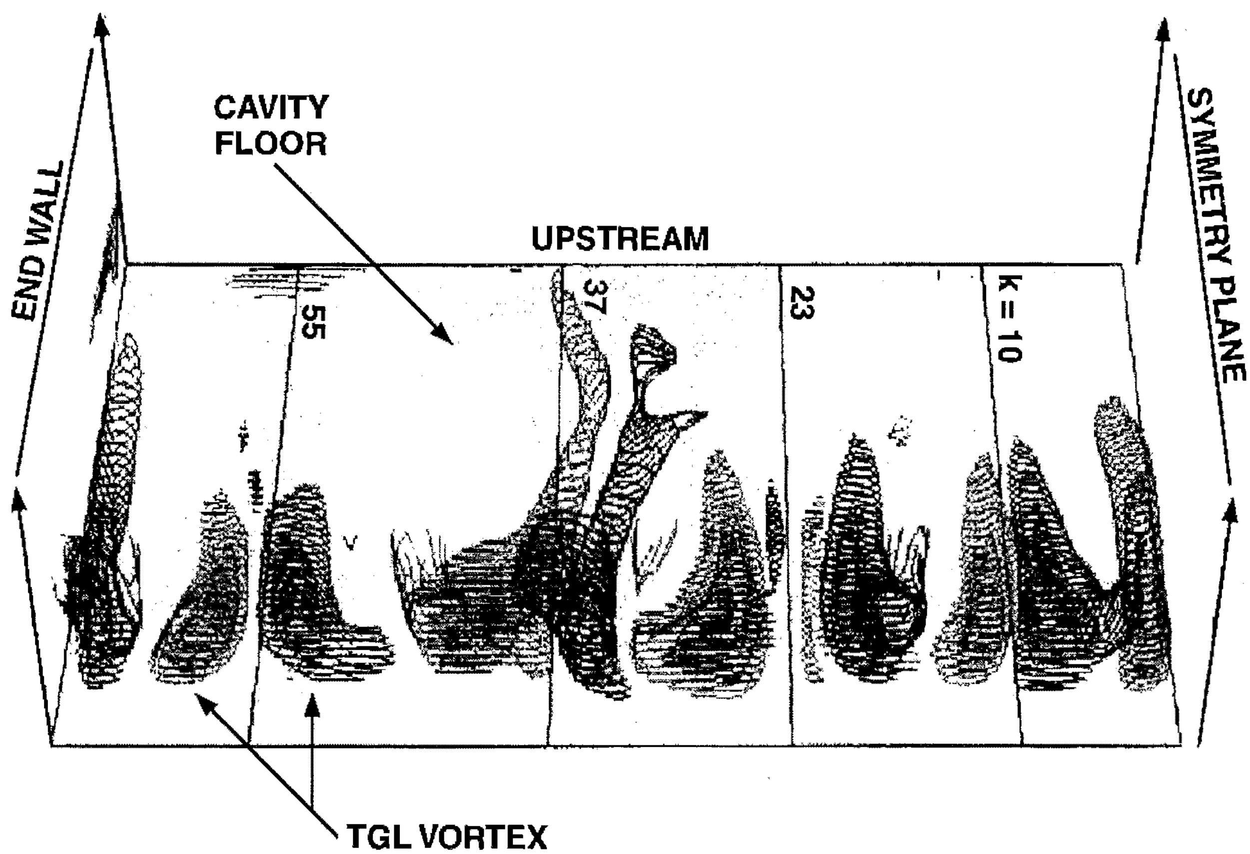

Figure 6. Spanwise Distribution and Streamwise Extent of TGL Vortices at Completion of DNS Computation (t = 3 min)

traces of a vertical and a horizontal velocity component and their power spectra for the Re = 5000 test case. The traces were extracted from recordings taken in the vicinity of the downstream free shear layer. For reference, the power spectra include Kolmogorov's slope of the inertial sub-range. Both spectra show numerous amplified frequencies, signifying an unsteady flow that is still deterministic. In figure 8 the computed mean horizontal velocity along the mid-span centerline is compared with the reported experimental data for SAR = 1:1 and SAR = 0.5:1 [26]. The DNS profile illustrates a further weakening of the "energy-sink" effect of the spanwise end-walls on the primary recirculation vortex core when the cavity SAR is extended to three.

As noted earlier, the DNS results of this test case helped to establish an acceptable form of the SGS turbulence model for the LES predictions. In particular, parametric studies were performed on the DNS results at intermittent time intervals to find a global set of values for Smagorinsky's constant (C_s) and the exponents (m and n) in the van Driest damping function. Furthermore, signs of transition first emerge within the downstream free shear layer [13]. By knowing this information a priori, it is also possible to perform quality checks on the model in terms of the turbulent eddy viscosity (TEV) magnitudes and distribution. In the following figures, the TEV magnitudes are normalized by the kinematic viscosity. Since the TGL vortices severely disturbed the basic features of the recirculating flow, the model quality was inspected only on planes lying between the spanwise vortex pairs.

The best set of fully-averaged correlation coefficients attained from the parametric study was $c_{11} = 0.30$, $c_{22} = 0.29$, and $c_{12} = 0.31$. The corresponding global model constants are $C_s = 0.1$, m = 8.0, and n = 0.14. Distribution of the c_{12} coefficient, plotted in figure 9, shows pockets of nearly perfect correlation close to the cavity walls and near the region of the downstream free shear layer. Notice that the poorest correlations occur primarily where the model TEV levels are expected to be low. As an example, see figure 10a where the highest TEV levels found in the individual recirculation planes are shown for the DNS results at completion of the simulation. This figure also reveals that the model predicts TEV magnitudes and distributions in accordance with the experimental observations. As a final note, the model quality was also checked against DNS results from a higher Reynolds number test case (Re = 7500) where the flow is locally transitional [13]. The highest TEV levels computed on the individual recirculation planes are shown in figure 10b. Indeed, the peak levels of TEV are concentrated within the downstream free shear layer.

LES RESULTS

The uniform grid selected for the LES computations at Re = 10,000 was 101 x 101 x 81. Based on the turbulent scales estimated by Koseff and Street [12] for the 3D cavity flow at Re = 10,000, this grid provides a higher spatial resolution than that needed to resolve Taylor's microscale. Shown in figures 11a and 11b are snapshots of the velocity field at sample time t = 6.5. The spanwise velocity vectors represent flow at the x = 0.77 plane, while the DSE region is shown at various planes between the TGL vortices. Besides the corner vortex, the spanwise velocity vectors show five additional vortex structures that appear distorted when compared with

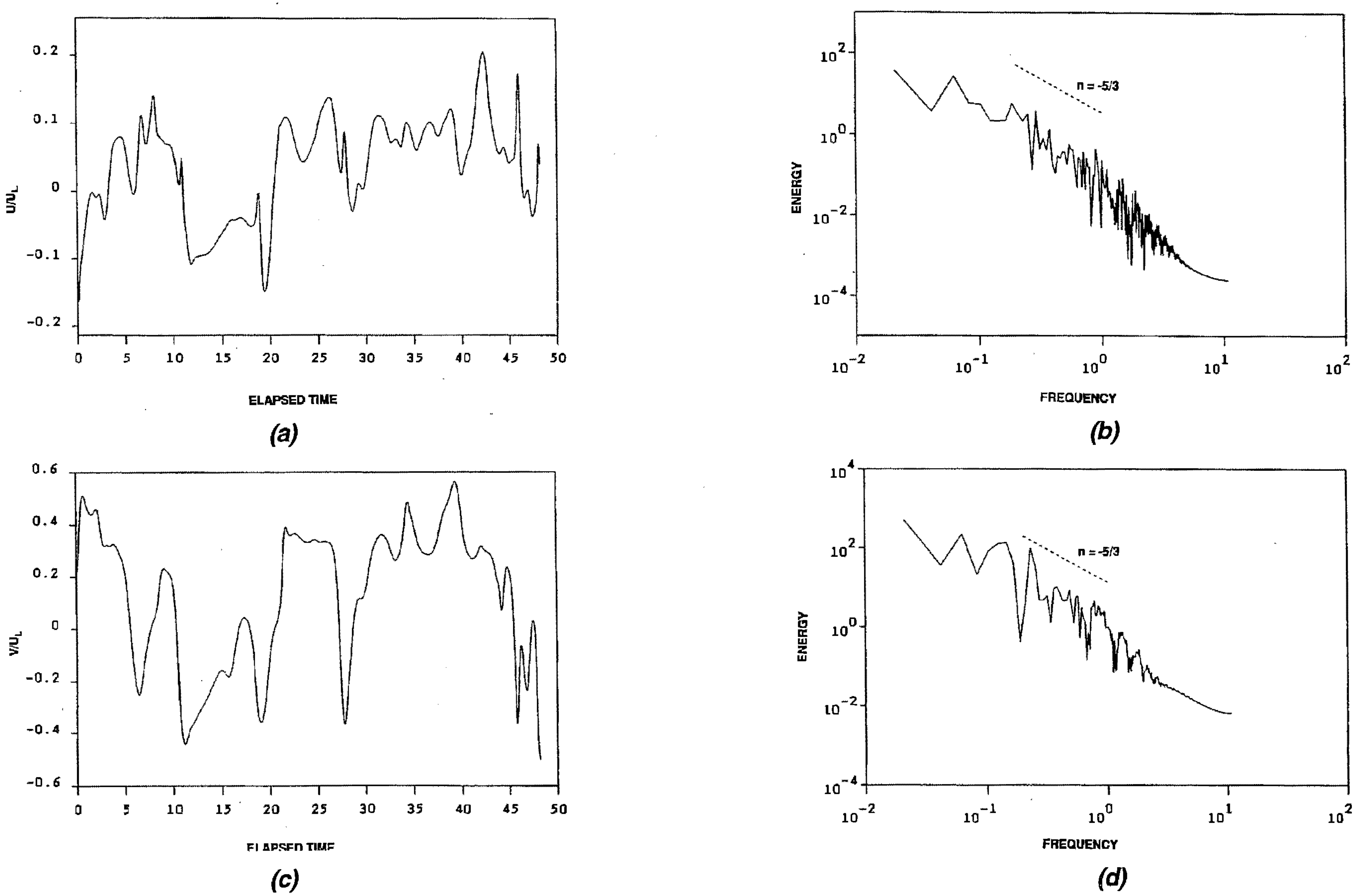

Figure 7. Time Traces (a) and (c) and Power Spectra (b) and (d) of Horizontal and Vertical Velocity Components Near the Downstream Free Shear Layer for Test Case Re = 5000

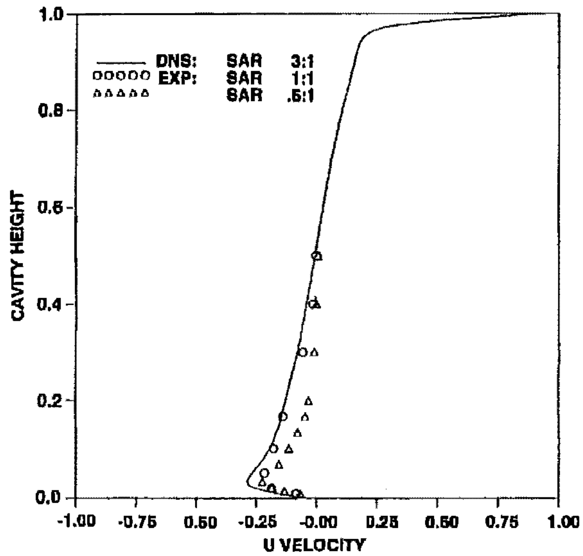

Figure 8. Quantitative Comparisons of the DNS Results and Experimental Data [26] in Terms of the Centerline Mean Velocities at the Cavity Mid-Span Plane

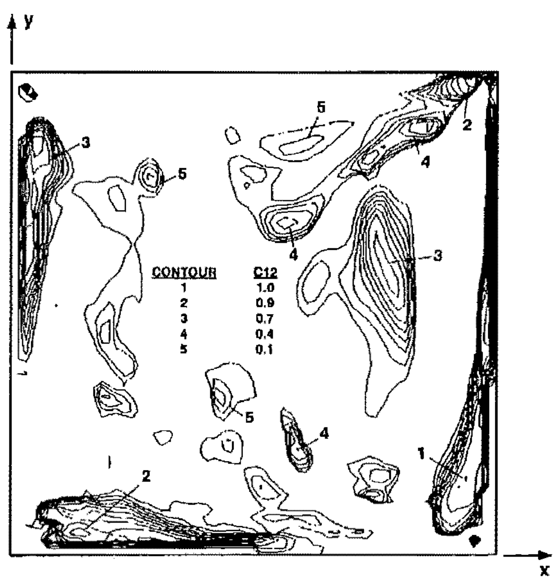

Figure 9. Distribution of Correlation Coefficient c_{12} Using $C_s = 0.1$ and Parameters $m = 8.0$ and $n = 0.14$ in Turbulence Length Scale Definition. Correlation Computed from DNS Data Taken at Completion of Test Case Re = 5000

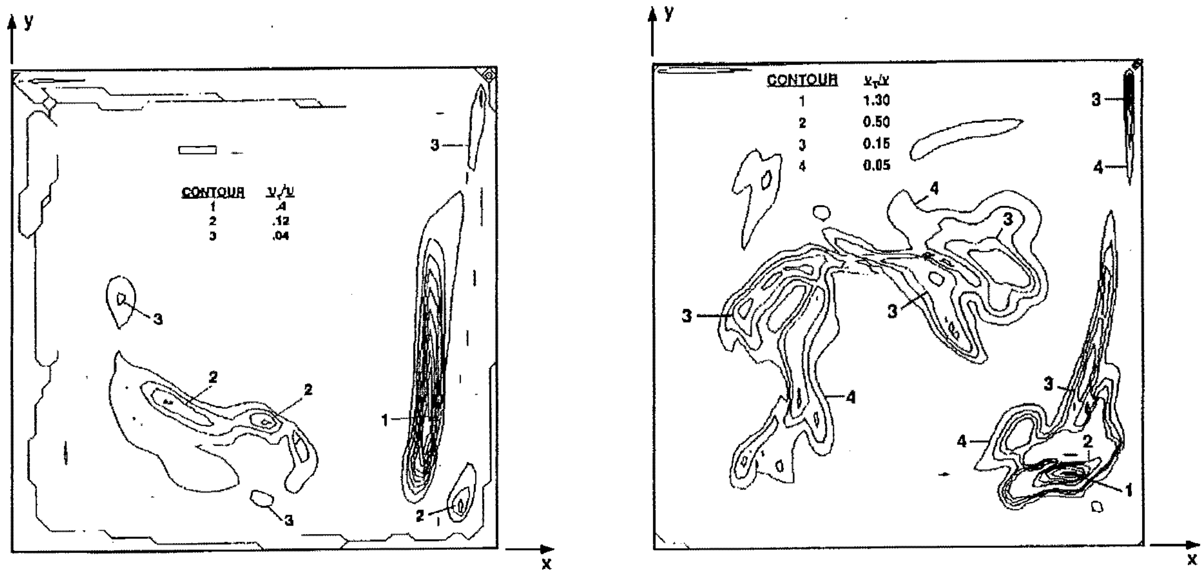

(a) (b)

Figure 10. Turbulent Eddy Viscosity Levels (Normalized by the Kinematic Viscosity) Computed from DNS Taken at Completion of Simulation; (a) Re = 5000 and (b) Re = 7500

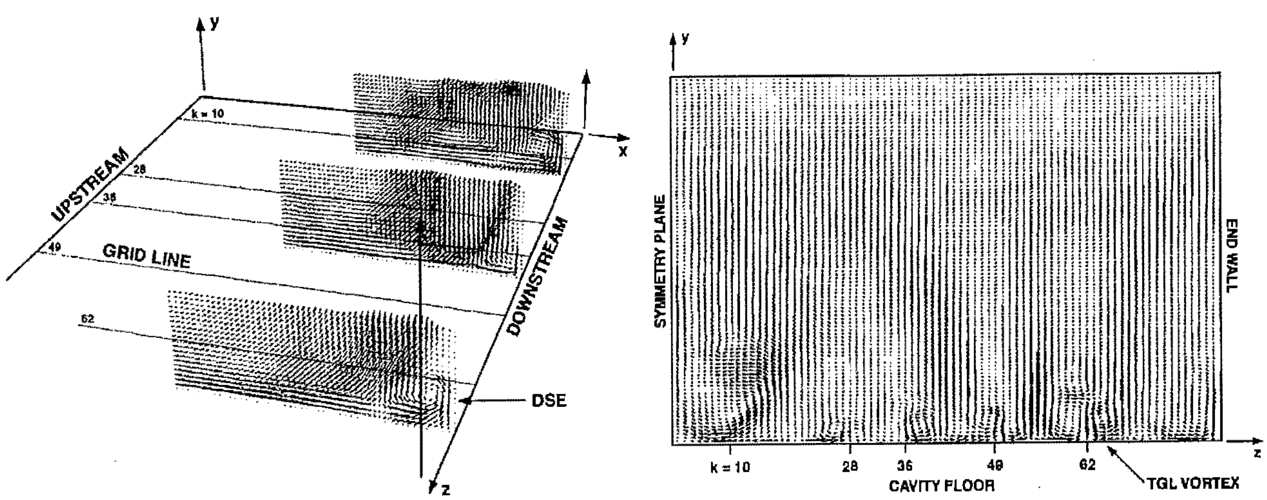

(a) (b)

Figure 11. Velocity Vectors Illustrating (a) Regions of the Downstream Secondary Eddy and (b) TGL and Corner Vortices for LES Test Case Re = 10,000 at Relative Time t = 6.5

the DNS results (Re = 5000). Breakdown of the TGL vortex structure is due to the onset of turbulence within the adjacent downstream free shear layers. Prasad and Koseff [26] (SAR = 1.0) and Koseff and Street [13] (SAR = 3.0) also reported a loss of TGL vortex structure at this Re, but they were unable to visualize the vortex flow patterns due to the rapid lateral dispersion of the dye streaks. The existence of the vortex structures and their streamwise extent is further illustrated in figures 12 and 13 in the form of stream function contours. Only results in the lower half of the cavity are shown. (The gridlines in the figures and in the velocity vectors (figure 11b) help quantify the intensity, spanwise size, and streamwise extent of each vortex.) The instability mechanism of TGL vortex generation still exists at this Re by evidence of the vortex structure created above the DSE between gridlines k = 49 and k = 62. Like the DNS results, neither the TGL vortices nor the corner vortex interact with the USE. Thus, the DSE structure remains intact throughout the cavity span. On the other hand, the irregular development of the DSE in the spanwise direction suggests complicated interactions between the unsteady effects of the primary recirculation vortex and the TGL vortices. As an example, Koseff and Street [17] and Prasad et al. [10] reported appearances of spiraling spanwise motions within the DSE, which they attributed to its interaction with the local vortices. Verification of their observations and the uncovering of other interactions are addressed next.

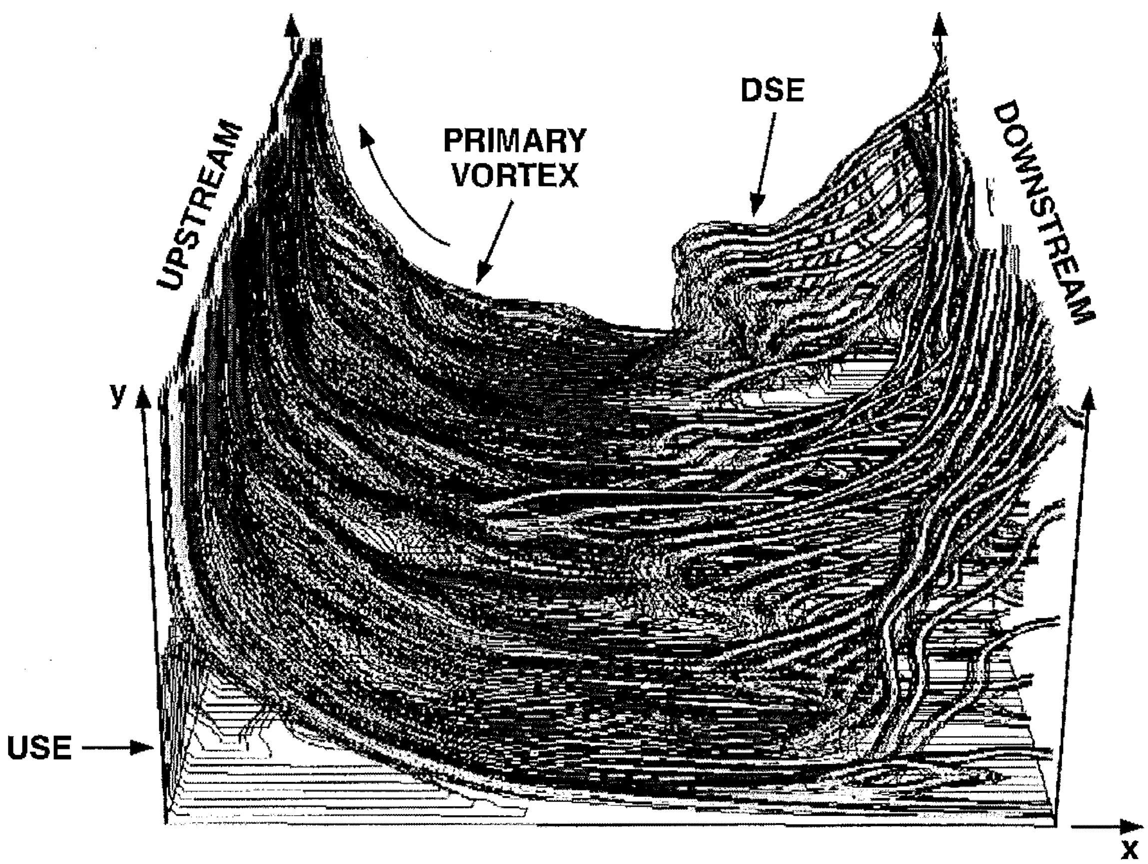

Figure 12. Stream Function Contours Showing the Downstream and Upstream Secondary Eddies of the Shear-Driven Cavity at Re = 10,000; Time t = 6.5

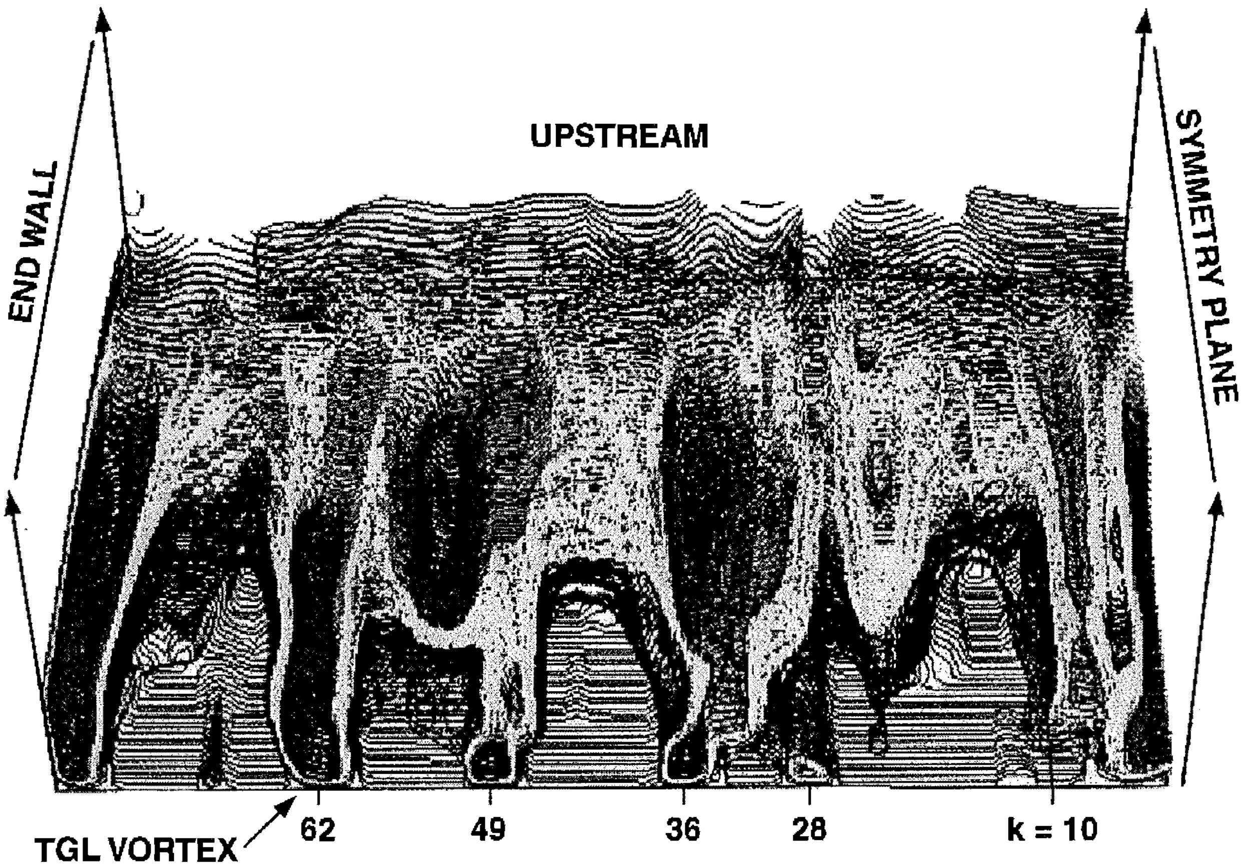

Figure 13. Stream Function Contours Showing the TGL and Corner Vortices of the Shear-Driven Cavity at Re = 10,000; Time t = 6.5

Between the spanwise vortices shown in figure 13, the streamlines form four surfaces that give a cave-like impression. Beneath these surfaces, the basic 2D structure of the DSE develops due to separation of the primary recirculation vortex from the downstream wall (see figure 11a). The vortices adjacent to the DSE strongly influence its spanwise characteristics. An attempt to understand these complicated characteristics, as well as the other flow features of the 3D cavity at Re = 10,000, is illustrated in figure 14 at sample time t = 6.5. In this figure, five sets of particle traces were initiated either within the DSE region or the outer extremes of the primary recirculation vortex, in particular, the first computational point off the downstream wall (x = 0.99). Also, each set originated halfway up the downstream wall (y = 0.5) except set 5, which started at y = 0.05. Set 1 contains three particle traces that were initiated directly over the center of the large TGL vortex (gridline number k = 10). After release, all three particles were entrained by the downwash flow of the large vortex. Their spiraling path then transversed streamwise only a short distance before being entrained by the upwash region of the vortex as given by the mid-span recirculation flow. Particles from sets 3 and 4 had a similar fate. Set 3 initiated above and to the left of the TGL vortex at gridline k = 28, while set 4 originated between the TGL vortices marked gridlines k = 28 and k = 36. Initially, each particle was convected by the primary recirculation vortex, which traced a path that coincides with the streamline

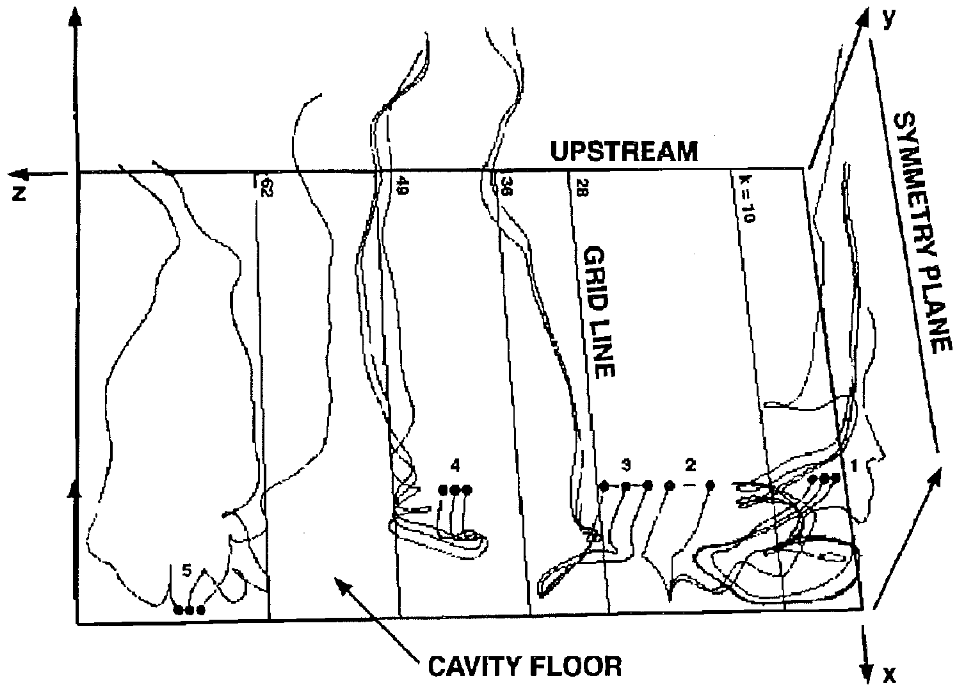

Figure 14. Five Sets of Particle Traces Illustrating the Interaction Among the Primary Recirculation Vortex, Downstream Secondary Eddy, and TGL and Corner Vortices of the LES Computation at Relative Time t = 6.5

surface shown in figure 12. As the particles neared the cavity bottom, they were entrained by the respective vortex instead of the DSE. The reason for this is illustrated by particle sets 2 and 5. Set 2 started above and to the right of the TGL vortex at gridline k = 28, while set 5 was centered just above the tiny flow structure that is positioned between gridline k = 62 and the end wall. As the particles of set 2 approached the cavity bottom, they were entrained by the DSE. However, because the large adjacent vortex induced a dominate spanwise velocity component on the DSE, the particles traced a broad spanwise spiral that turned quickly streamwise once fully entrained by the vortex. This spanwise spiral within the DSE region is also traced by particle set 5. From these observations, we can conclude that the streamwise extent of the TGL vortex structures shown in figure 13 are sustained through two patterns of fluid entrainment. Close to the downstream wall, these vortices entrain fluid from the adjacent DSE regions, which in turn extract fluid from the primary recirculation vortex. As mentioned earlier, this flow pattern was also observed locally in the 3D cavity in the flow visualization experiments. Upstream from the DSE region, however, the TGL vortices entrain fluid from the primary vortex directly. Loss of the vortex structure occurs upstream once the primary vortex separates from the cavity bottom. Having this understanding, the tiny flow structure within the DSE region between gridline k = 62 and the span's end wall is another vortex pair. Creation of this secondary vortex pair is due to the opposing spanwise viscous interactions of the corner vortex, the adjacent TGL vortex, and the no-slip condition along the cavity bottom. Above its center position lies an imaginary surface within the DSE region that demarcates fluid entrained by the corner vortex apart from that extracted by the adjacent TGL vortex. The existence of this flow surface is illustrated by the right and left particle traces in set 5. As shown in figure 14, the spanwise spiral trace of each

particle is in opposite directions. Thus, these particles started on opposite sides of the flow surface. Because the adjacent TGL vortices change size and meander along the cavity floor over time, the flow surfaces and corresponding secondary vortices are not stationary. As a matter of fact, flow visualizations of the numerical results showed extremely complicated dynamics that governed these tiny structures. However, their impact on momentum and energy transfer throughout the cavity was never significant.

Now the effects of the symmetry plane assumption on these LES results will be discussed. Koseff and Street [12] noted that the mean recirculation flow in the 3D cavity with SAR = 3.0 became self-similar when the Reynolds number was increased to 10,000. By examining the comparisons between the computed centerline mean velocity profiles and the experimental results in figures 15a and 15b, one can see that this is indeed the case. While the experimental data are at the mid-span plane, the computed profiles are shown along the centerline of the recirculation plane $z = 0.28$ (K15 plane); $z_{max} = 1.5$. In both profiles, the averaged error (as compared with the data) is less than 2 percent. Thus, the symmetry plane assumption has a negligible effect on the mean recirculation at the K15 plane and throughout the remainder of the cavity span. Unfortunately, no centerline Reynolds stresses or turbulent velocity fluctuations of the 3D cavity flow with SAR = 3.0 were published. However, data were reported by Prasad and Koseff [26] at the mid-span plane for SAR = 1.0. Quantitative comparisons of those data and the LES results at the mid-span, K15, and end planes are shown in figures 16a and 16b in terms of the centerline root-mean-square (RMS) velocity fluctuations. The end plane profile in each figure was computed at recirculation plane $z = 1.25$. Both figures clearly show large discrepancies between the computed and experimental mid-span plane RMS results. Conversely, RMS profiles at the K15 and end planes agree reasonably well with each other, as well as with the experimental mid-span plane data. Furthermore, the computed profiles extend the overall observed trend that turbulent kinetic energy is lost near the cavity walls when the cavity SAR is reduced [17,26]. Hence, for this test case, these observations along with the experimental agreement of the computed mean recirculation flow illustrated a localized effect of the spanwise symmetry plane assumption on the LES results.

As final issues to address, do these LES computations support the explicit understanding that turbulence dominates the flow characteristics near the downstream free shear layer, and at this Reynolds number what are the spatial distributions of the velocity fluctuations elsewhere in the cavity? Figures 17a and 17b show the energy spectrum of the velocity fluctuations calculated from a 90-second sample record taken in the vicinity of the downstream free shear layer. Both spectral profiles display an inertial subrange with about an order of magnitude larger energy content within the vertical fluctuations. This result, as well as the bandwidth over which the inertial subrange occurs, agrees with similar analyses conducted on the experimental data [12]. In figures 18a and 18b, distributions of the vertical RMS fluctuations and shear stress component $\overline{u'v'}$ at the K15 plane indeed disclose highest levels within the downstream free shear layer region. However, one should note that the RMS levels of the vertical velocity fluctuation are also significant along the downstream wall.

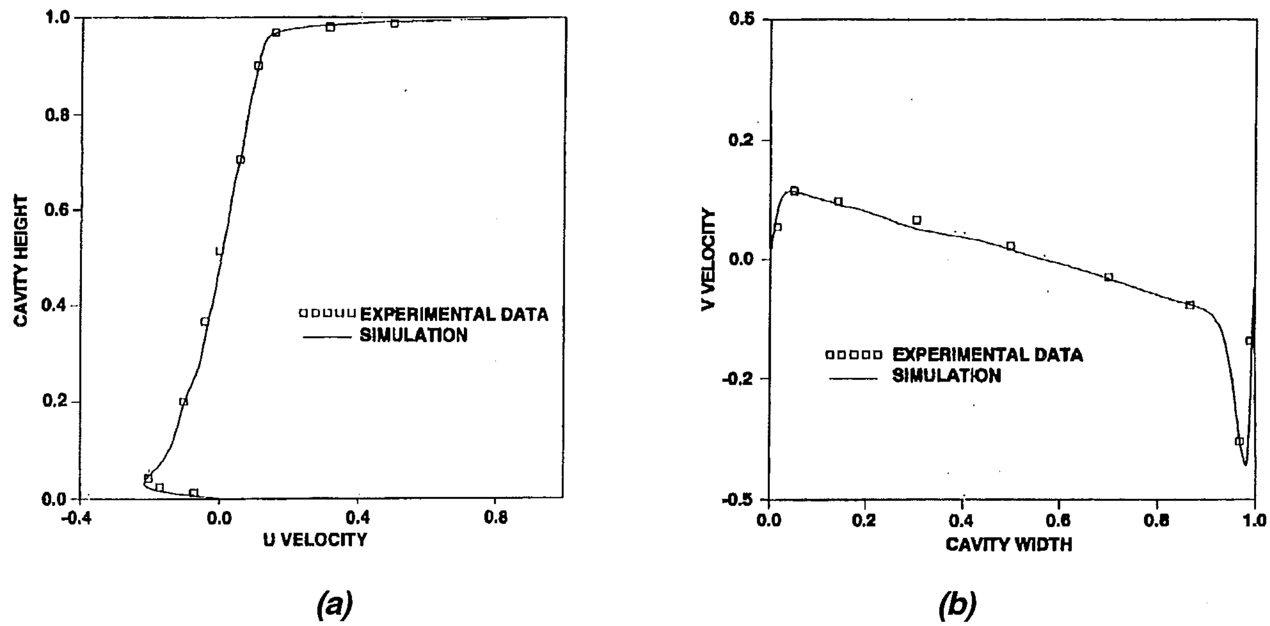

Figure 15. Comparison of LES and Experimental Results [12] in Terms of Centerline Mean Velocity Profiles; Simulation Profile at K15 Plane and Experimental Data Measured at Mid-Span Plane

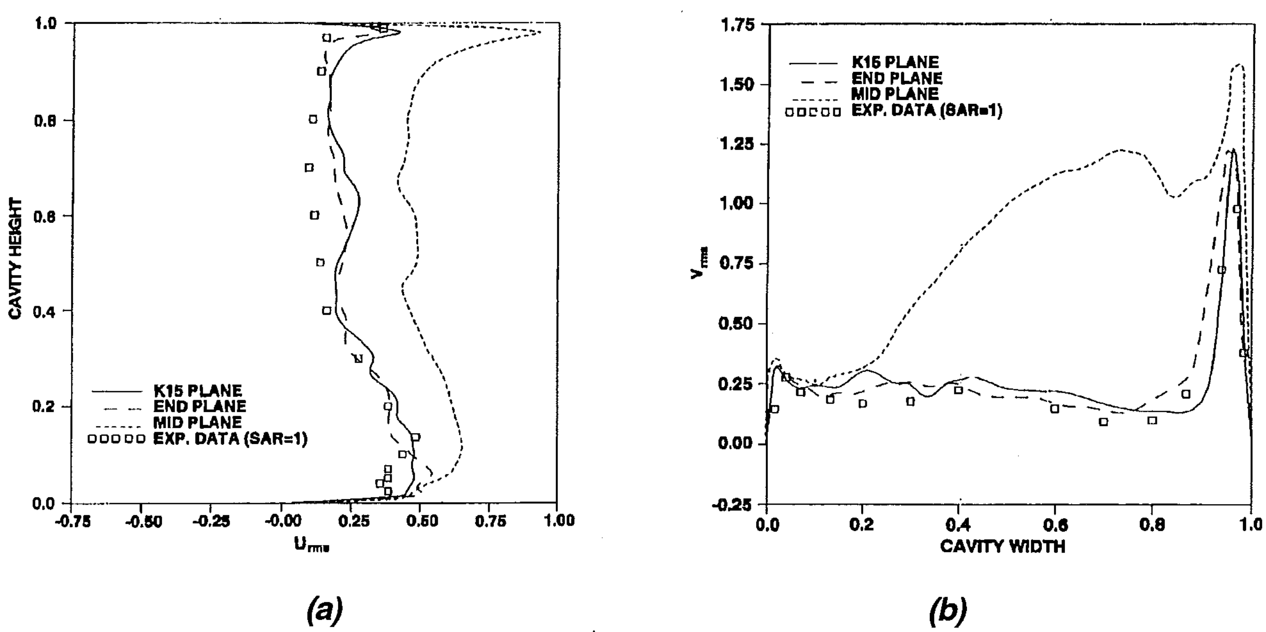

Figure 16. Profiles of Centerline Horizontal and Vertical RMS Velocity Fluctuations; LES Profiles are at the K15, End, and Mid-Span Planes While Experimental Data Are at the Mid-Span Plane of Cavity with SAR = 1:1

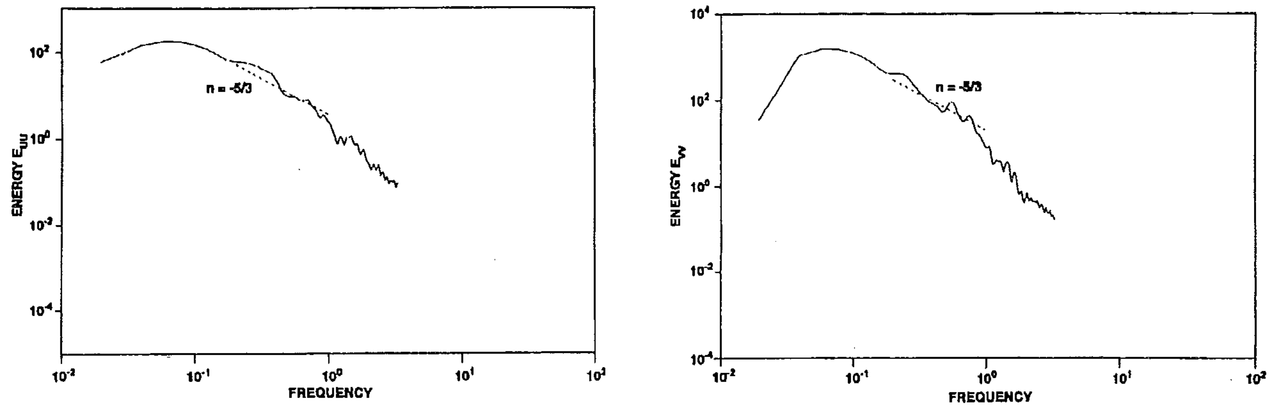

(a) *(b)*

Figure 17. Power Spectra of Velocity Components Near the Downstream Free Shear Layer; (a) Horizontal, (b) Vertical

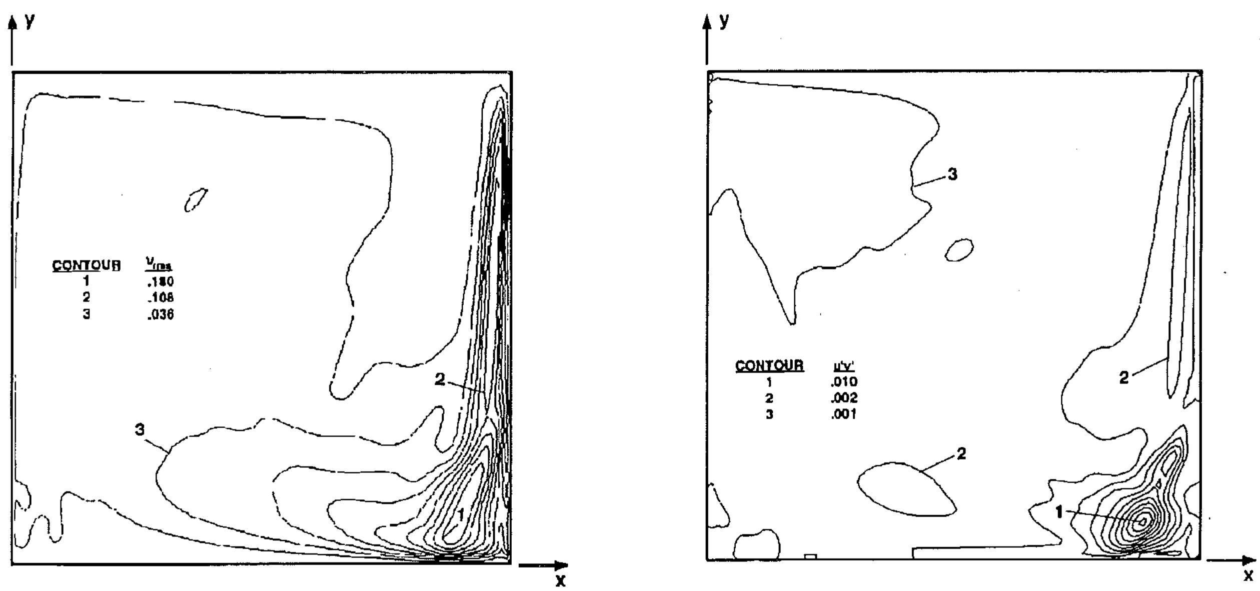

(a) *(b)*

Figure 18. Distribution of the (a) Vertical RMS Fluctuations and (b) $\bar{u}'\bar{v}'$ Shear Stress Component at the K15 Plane

CONCLUSIONS

Direct numerical simulation (DNS) and large-eddy simulation (LES) methodologies are used to study the unsteady and turbulent characteristics of the three-dimensional shear-driven cavity flow at Reynolds numbers 5000 and 10,000. Based on the numerical results, the following conclusions about this flow are offered:

1. At Re = 5000 (DNS results), the flow is laminar, but the three-dimensionality and unsteadiness severely disturbs the basic structure of the classic recirculation flow features. The TGL vortices change rapidly in size and they meander only locally. We predicted nine TGL vortex pairs spanning the cavity bottom, with one straddling the mid-span plane. The flow remains fully deterministic. Since the onset of turbulence occurs between Reynolds numbers of 6000 and 8000 [12], these results provided a reasonable means for determining the global parameters in the SGS length scale definition.

2. At Re = 10,000 (LES results) the instability mechanism for TGL vortex generation still exists, but the vortices themselves have now become distorted due to the onset of turbulence within the downstream free shear layer. Their physical characteristics throughout the 3D cavity vary randomly. The combined effects of the primary recirculation vortex and the TGL and corner vortices cause a complicated irregular development of the DSE. Near the downstream wall the TGL vortices extract fluid from the downstream eddy region, which concurrently entrains fluid from the primary recirculation vortex. Upstream of the downstream eddy region, the TGL vortices entrain fluid directly from the primary vortex. Lastly, secondary vortex pairs are created intermittently within the DSE region due to the viscous interactions among the adjacent larger vortices and the cavity floor.

REFERENCES

1. U. Ghia, K.N. Ghia, and G.T. Shin, "High-Re Solutions of Incompressible Flow Using the Navier-Stokes Equations and a Multigrid Method," J. Comp. Phys., Vol. 48, 1982, pp. 387-411.

2. K. Gustafson and K. Halasi, "Vortex Dynamics of Cavity Flows," J. Comp. Phys., Vol. 64, No. 2, 1986, pp. 279-319.

3. A.D. Gosman, W.M. Pan, W.M. Runchal, D.B. Spaulding, and M. Wofshtein, Heat and Mass Transfer in Recirculating Flows, Academic Press, London, 1969.

4. D.L. Young, J.A. Liggett, and R.H. Gallagher, "Unsteady Stratified Circulation in a Cavity," J. Eng. Mech. Div., ASCE 102, EM6, 1976, pp. 1009-1023.

5. F.J.K. Ideriah, "On Turbulent Forced Convection in a Square Cavity," Numer. Meth. in Lam./Turb. Flow, Proc. 1st Int'l. Confer., 1978, pp. 257-269.

6. P.H. Gaskell, and A.K.C. Lau, "The Method of Curvature Compensation and its Use in the Prediction of Highly Recirculating Flows," AIAA/ASME/SIAM/APS 1st Nat. Fluid Dyn. Cong., 1988, pp. 272-279.

7. W.Y. Soh and J.W. Goodrich, "Unsteady Solution of Incompressible Navier-Stokes Equations," J. Comp. Phys., Vol. 79, 1988, pp. 113-134.

8. P. Moin and J. Kim, "On the Numerical Solution of Time-Dependent Viscous Incompressible Fluid Flows Involving Solid Boundaries," J. Comp. Phys., Vol. 35, 1980, pp. 381-392.

9. C.J. Freitas, R.L. Street, A.N. Findikakis, and J.R. Koseff, "Numerical Simulation of Three-Dimensional Flow in a Cavity," Inter. J. Numer. Meth. Fluids, Vol. 5, No. 6, 1985, pp. 561-576.

10. A.K. Prasad, C.Y. Perng, and J.R. Koseff, "Some Observations on the Influence of Longitudinal Vortices in a Lid-Driven Cavity Flow," AIAA/ASME/SIAM/APS 1st Nat. Fluid. Dyn. Congr., 1988, pp. 288-295.

11. S.A. Jordan and S.A. Ragab, "An Efficient Fractional-Step Technique for Unsteady Three-Dimensional Flows," J. Comp. Phys. (in review).

12. J.R. Koseff and R.L. Street, "The Lid-Driven Cavity Flow: A Synthesis of Qualitative and Quantitative Observations," J. Fluids Engr., Vol. 106, No. 1, 1984, pp. 390-398.

13. J.R. Koseff and R.L. Street, "Visualization Studies of a Shear Three-Dimensional Recirculating Flow," J. Fluids Engr., Vol. 106, No. 1, 1984, pp. 21-29.

14. G.I. Taylor, "Stability of Viscous Liquid Contained Between Two Rotating Cylinders," Phil. Trans. Roy. Soc. (London), Vol. 223, pp. 289-343.

15. H. Görtler, "On the Three-Dimensional Instability of Laminar Boundary Layers on Concave Walls," NACA Tech. Memor. 1375, 1954.

16. H.S. Rhee, J.R. Koseff, and R.L. Street, "Flow Visualization of a Recirculating Flow by Rheoscopic Liquid and Liquid Crystal Techniques," Exper. Fluids, Vol. 2, 1984, pp. 57-64.

17. J.R Koseff and R.L. Street, "On End Wall Effects in a Lid-Driven Cavity Flow," J. Fluids Engr., Vol. 106, No. 1, 1984, pp. 385-389.

18. V. deBrederoede and P. Bradshaw, "Three-Dimensional Flow in Nominally Two-Dimensional Separation Bubbles, I. Flow Behind a Rearward Facing Step," I. C. Aero Report 72-19, 1972.

19. J. Kim and P. Moin, "Application of a Fractional-Step Method to Incompressible Navier-Stokes Equations," J. Comp. Phys., Vol. 59, 1985, pp. 308-310.

20. R.A. Clark, J.H. Ferziger, and W.C. Reynolds, "Evaluation of Subgrid-Scale Turbulence Models Using an Accurately Simulated Turbulent Flow," J. Fluid Mech., Vol. 91, 1977, pp. 1-16.

21. S.V. Patankar, Numerical Heat Transfer and Fluid Flow, Hemisphere, Washington, DC, 1980.

22. S.A. Jordan, "An Iterative Scheme for Numerical Solution of Steady Incompressible Viscous Flows," Comp. Fluids, Vol. 21, No. 4, 1992, pp. 503-517.

23. J. Smagorinsky, "General Circulation Experiments with the Primitive Equations, I. The Basic Experiment," Mon. Wealth. Rev., Vol. 91, 1963, pp. 99-164.

24. E.R. van Driest, "On the Turbulent Flow Near a Wall," J. Aero. Sci., No. 23, 1965, pp. 1007-1011.

25. U. Piomelli, J.H. Ferziger, and P. Moin, "Model for Large Eddy Simulation of Turbulent Channel Flow Including Transpiration," Dept. of Mech. Engr. Report TF-32, Stanford U., Stanford, CA, 1988.

26. A.K. Prasad and J.R. Koseff, "Reynolds Number and End-Wall Effects on a Lid-Driven Cavity Flow," Phys. Fluids, A1 (2), 1989, pp. 208-218.

DISTRIBUTION LIST

External

ONR (P. Purtel, K. Ng)

Internal

Codes:	02244
	0251
	0261 (NLON Library)
	0262 (NPT Library(2))
	10
	102 (Lima)
	22
	38
	3891
	411
	80
	81
	821
	83
	832
	8322 (Jordan (5))
	833 (Cayer)
Total:	24